J. COMBIN. MATH. COMBIN. COMPUT. 127a (2025) 3997--4022

Journal of Combinatorial Mathematics and Combinatorial Computing
www.combinatorialpress.com/jcmcc

Comparison of Multi-Technology Routes and Construction of Virtual Simulation Environment for Energy Storage Power Station Using 3D Visualization Technology

Shaohua Zhao[1,✉], Jiasheng Wu[1], Chao Dong[1], Junyu Zhu[1], Liangrui Zhou[1], Yi Yang[1]

[1] *CGS POWER GENERATION(GUANGDONG)ENERGY STORAGE TECHNOLOGY CO., LTD, Guangzhou, Guangdong, 510630, China*

ABSTRACT
This paper constructs a three-dimensional model of energy storage power station through three-dimensional visualization technology, and builds a virtual simulation environment of energy storage power station by inputting realistic environmental parameters. Four different energy storage technology routes, namely lithium-electronic battery energy storage, lead-acid battery energy storage, pumping energy storage and air compression energy storage, are selected, and the energy storage performance of the four technology routes is explored in depth based on the constructed virtual environment. At the same time, the energy storage performance of four different technology routes in the virtual environment of the energy storage power station is compared using the energy storage capacity and energy storage efficiency as the measurement indexes, and the energy storage technology routes suitable for the environment of this paper are highlighted based on the comparison results. In the energy storage simulation, the net energy storage capacities of the four technology routes in the virtual environment of this paper are 728.99MW, 724.18MW, 461.50MW and 393.45MW, respectively. Compared with the other three energy storage technology routes, the lead-acid battery energy storage capacity fluctuation is smaller, and the energy storage capacity is higher, with a higher degree of adaptability to the virtual simulation environment in this paper. At the same time, the average energy storage efficiency of lead-acid battery in four quarters is 99.71%, compared with the next highest efficiency of lithium-electronic battery energy storage efficiency increased by 14.29%, which further indicates that the lead-acid battery energy storage technology route in this paper builds the best performance of the virtual simulation environment of the energy storage power station.

Keywords: three-dimensional visualization, lead-acid battery energy storage, energy storage capacity, energy storage efficiency, energy storage power station

1. Introduction

In recent years, computer network technology has been developing vigorously, which also promotes the development and progress of related industries and technologies, and “virtual reality” technology is one of them. Virtual reality technology using computer technology and modern electronic technology to generate visual, auditory, tactile integration of the virtual environment, the user using

✉ Corresponding author.
E-mail address: cnkjzhaoshaohua@126.com (S. Zhao).
Received 12 January 2024; Revised 25 March 2024; Accepted 25 December 2024; Published Online 15 April 2025.
DOI: 10.61091/jcmcc127a-226

specific equipment can be very natural and the virtual environment to interact, thus producing immersive feelings and experiences, is a sense of immersion, interactivity and imagination of human-computer interaction technology [1-4]. As an important branch of virtual reality technology, three-dimensional visualization technology breaks through the traditional way of displaying information, and intuitively and three-dimensionally presents the complicated data and information obtained from the real world to the users in a three-dimensional visualization way [5-7]. Three-dimensional visualization technology is not only able to express spatial data and feature information, but also can display data information obtained from the real world in an all-round and multi-angle way, which is more advantageous from both the spatial dimension and the inter-inch dimension [8-10].

At present, there are still some difficult to solve problems in the operation and management process of energy storage power stations. On the one hand, the planning information management of hydropower stations still adopts the form of flat data such as digital maps and text files, which results in the consequences of low management efficiency, inconvenient information query, and poor display effect [11-12]. Secondly, the dispersed information and lack of corresponding information sharing and management platform in each department of the storage power station have led to the low level of information management of the hydropower station, low work efficiency, and indirectly caused quite huge economic losses [13-14]. Therefore, the construction of digital, information-based three-dimensional visualization system for energy storage power stations, using the three-dimensional model of the three-dimensional sense and vivid expressiveness to describe the real world is far more intuitive, vivid, reliable and efficient than two-dimensional plane information.

Xia, P. elucidated the pain points of traditional power system operation and maintenance, which relies heavily on sensors to measure parameters and relay actions, resulting in the inability to intuitively display information about the operating status of the power system, whereas the 3D visualization technology can identify and display the 3D model of the physical image of the power equipment, assisting the operation and maintenance managers to make decision-making analyses [15]. Dongyun, D. et al. utilized industrial internet and digital twin technology to correlate the three-dimensional model of hydrogen production and storage power station equipment with instance data to construct an intelligent operation and maintenance system that can connect the equipment operation status and operation environment in real time, which effectively prevents safety hazards during the operation of the power station [16]. Li, Y. et al. proposed an interactive online 3D visualization framework capable of integrating and visualizing multi-source grid information from the power station to the system and reducing the model loading time while improving the model rendering accuracy by generating a multi-level-of-detail (LoD) structure of the grid facilities [17]. Gan, X. et al. evaluated the application of a 3D visualization system for digital power grid engineering and introduced the engineering hierarchical model based on the visualization system as well as the technology-related techniques and development environment respectively, and found that the system can effectively improve the efficiency and intelligence of power grid engineering through example investigations [18]. Tang, X. et al. applied the Unity-based 3D visualization technology of grid wiring diagrams to the grid dispatch system, which not only improved the efficiency of grid wiring diagram generation by integrating geographic information, but also fully demonstrated the operational status of the grid scene and provided a friendly human-computer interaction experience [19]. Wang, H. et al. constructed a 2D drawing recognition program integrating augmented reality and 3D visualization technologies to superimpose a 3D model on top of the drawing, which not only reduces the operator's work error situation during the nuclear power construction and maintenance process, but also provides a new experience and implementation plan for equipment and plant maintenance analysis, preview and personnel training [20]. Dai, E. et al. designed a dynamic visualization system for offshore wind farms based on a data fusion method to build windmill models and geographic matrix models with the help of the Unity3D game engine, and real-time data communication through PhotonServer, which ultimately realizes real-time 3D reconstruction of wind farms [21]. Qian, P. et al. to meet the development needs of the electric power industry, proposed a design scheme for a multi-station integrated visualization system based on digital twin technology, which utilizes artificial intelligence and virtual reality technology to realize the data transmission between physical entities and virtual models of multiple substations in order to complete the unified management and monitoring of multiple substations [22].

This paper focuses on lithium-ion battery energy storage, lead-acid battery energy storage, pumped storage and compressed air energy storage as the energy storage power station technology routes involved in the comparison, and explores its energy storage performance in the virtual simulation environment of the energy storage power station built in this paper. Through the real-life energy storage power station data collection and other work, this paper utilizes 3dsMax software for the construction of the three-dimensional model of the energy storage power station. Aiming at the problem of complex structure and numerous components of the energy storage power station, this paper introduces comprehensive modeling methods such as face-sheet modeling and polygonal modeling to carry out three-dimensional visualization modeling of the components of the energy storage power station with different degrees of complexity. The construction of the virtual scene is completed by using various functional components that come with Unity3D, and the collision test algorithm suitable for the scene in this paper is selected through the test comparison of the hierarchical enclosing box (Rapid) algorithm, the improved Rapid algorithm and the improved Rapid algorithm with the omission of preprocessing. Based on the virtual simulation environment of the completed energy storage power station, this paper explores the energy storage performance of various energy storage technology routes such as lithium-ion battery energy storage one by one, and examines the energy storage performance of different technology routes in the virtual environment of this paper. In order to highlight the difference between the energy storage performance of different technology routes, and explore the technology routes suitable for the virtual environment of this paper. In this paper, we compare and analyze the different results of the four energy storage technology routes using energy storage capacity and energy storage efficiency as the indicators. According to the data obtained, the performance of different technology routes and the suitability of the virtual simulation environment of the energy storage power plant constructed in this paper are explained.

2. Multi-technology route for energy storage power stations

2.1. Lithium-Electronic Battery Energy Storage

Lithium-ion batteries are batteries with lithium metal or lithium alloy as the anode material and using a non-aqueous electrolyte solution. The negative electrode of lithium batteries usually consists of graphite-like materials [23]. The diaphragm is usually a polyethylene film or polypropylene film, or a composite film of both, and the electrolyte is mainly lithium hexafluorophosphate. The charging and discharging process of lithium batteries mainly relies on the movement of lithium ions (Li+) between the positive and negative electrodes. When charging, lithium ions are de-embedded from the positive electrode, embedded in the negative electrode through the electrolyte, and the negative electrode is in a lithium-rich state, forming lithium metal or lithium ion compounds and storing energy. Lithium ions move from the negative electrode to the positive electrode and react with metal oxides or other compounds on the positive electrode to release energy. The entire process is reversible, so lithium-ion batteries can be charged and discharged repeatedly.

Take lithium cobaltate $\left(LiCoO_2\right)$, the cathode material and graphite $\left(C\right)$, the anode material of commonly used lithium-ion batteries, as an example, the reaction equation on the cathode and on the anode of lithium-ion batteries is equation (1):

$$\begin{aligned}&\text{Positive: LiCoO}_2 \rightarrow \text{Li}_{1-x}\text{CoO}_2 + x\text{Li} + xe- \\ &\text{Negative: } x\text{Li} + + xe- + C \rightarrow Li_xC\end{aligned} \tag{1}$$

When the battery is charging, the voltage applied by the external power source causes a chemical reaction to occur inside the battery, migrating lithium ions from the negative pole to the positive pole, with the graphite material on the negative pole being inserted by lithium ions, and the lithium cobaltate material on the positive pole being dislodged by lithium ions, and releasing electrons at the same time, which ultimately fills the battery. When the battery is discharged, the positive and negative electrode chemical reaction is reversed, electrons flow from the negative electrode to the positive electrode, and lithium ions migrate from the positive electrode to the negative electrode, releasing the stored energy. The reaction equation of the whole battery can be expressed as equation (2):

$$\begin{aligned}&\text{Charge: } LiCoO_2 + C \rightarrow Li_{1-x}CoO_2 + Li_xC \\ &\text{Discharge: } Li_{1-x}CoO_2 + Lix_{C1} \rightarrow LiCoO_2 + C\end{aligned} \tag{2}$$

2.2. *Lead-acid battery energy storage*

Lead-acid batteries are commonly known as electric batteries, and their monoblocks are mainly composed of positive and negative plates, separators, electrolyte, safety valves, terminals, battery casing and other components [24]. Among them, the positive plate is lead oxide and the negative plate is spongy lead. Dilute sulfuric acid is used as the electrolyte to transfer electrons between the positive and negative plates. Ultrafine glass fiber wool is used as the spacer, and the electrolyte is adsorbed in the spacer, and there is no flowing electrolyte inside the battery. At the same time, the porous structure of the separator makes the electrolyte flow back and forth between the positive and negative plates, and the active substances on the plates can fully react with the electrolyte. The safety valve is made of high quality acid-resistant and anti-aging synthetic rubber, when the air pressure inside the battery rises, the safety valve opens automatically and discharges the gas, so that the air pressure inside the battery is maintained within a certain value. The shell is made of resin fiber, which protects the battery and provides space for positive and negative plates. Battery terminals are used to connect the battery to external circuits. Depending on the type of battery, the terminals can be connecting tabs, connecting rods or lead wires.

Lead-acid batteries store or release energy through a redox reaction between the positive and negative plates. Its charging and discharging process is divided into a reversible primary reaction and an irreversible secondary reaction:

Positive electrode:

$$PbSO_4 + 2H_2O \underset{\text{Discharge}}{\overset{\text{Charge}}{\rightleftharpoons}} PbO_2 + H_2SO_4 + 2H^+ + 2e^- \tag{3}$$

Side effects:

$$2H_2O \xrightarrow{\text{Charge}} O_2 + 4H^+ + 4e^- \tag{4}$$

$$Pb + 2H_2O \xrightarrow{\text{Charge}} PbO_2 + 4H^+ + 4e^- \tag{5}$$

Negative:

$$PbSO_4 + 2H^+ + 2e^- \underset{\text{Discharge}}{\overset{\text{Charge}}{\rightleftharpoons}} Pb^+H_2SO_4 \tag{6}$$

Side effects:

$$2H^+ + 2e^- \xrightarrow{Charge} H_2 \tag{7}$$

During charging, reactions (3) and (6) proceed in the positive direction, where lead sulfate on the positive and negative electrode plates reacts with water to form lead dioxide, lead and dilute sulfuric acid. The conversion rate is very high at the beginning, which is due to the drastic increase of sulfuric acid formed within the micropores of the polar plates, too late to diffuse outward, when the terminal voltage rises rapidly. In the middle of charging, the sulfuric acid in the polar plate begins to diffuse outward, when the rate of increase of sulfuric acid in the micropores of the polar plate and the rate of diffusion tends to balance, the charging acceptance rate decreases, and the end voltage rise slows down. In the late charging stage, most of the lead sulfate on the polar plate is converted to lead dioxide and spongy lead, and if charging is continued, the side reaction occurs, and equations (4), (5) and (7) are carried out in the positive direction. Water decomposition produces large amounts of hydrogen and oxygen. If charging continues, the active material on the pole plate is all reduced to lead dioxide and lead, water decomposition also tends to saturation, the charging acceptance rate further decreases, and the end voltage gradually tends to level off.

At the beginning of the discharge, reaction (3) and (6) reverse, lead dioxide on the positive plate reacts with sulfuric acid to produce water, the electrolyte concentration in the microporous pole plate drops rapidly, and the terminal voltage drops. In the middle of the discharge, the electrolyte outside the pole plate spreads to the pole plate microporous, which slows down the decrease of the electrolyte concentration in the microporous, and the drop of the terminal voltage slows down at this time. At the end of the discharge, most of the lead dioxide and spongy lead on the positive and negative electrode plates become lead sulfate, and the lead sulfate blocked on the electrode plate and in the microporous microporous electrolyte is difficult to penetrate into the electrolyte outside of the electrode plate due to its large volume. Therefore, the electrolyte with lower concentration in the microporous is difficult to mix with the electrolyte outside the electrode plate, and the terminal voltage drops very quickly. The charging and discharging curves of lead-acid batteries are shown in Figure 1. During the charging and discharging process of lead-acid batteries, the more active substances are generated or consumed, the more power is stored in the lead-acid battery, and the stronger the power storage capacity is, i.e., the capacity of lead-acid batteries depends on the amount of active substances on the positive and negative electrode plates and the concentration of electrolyte.

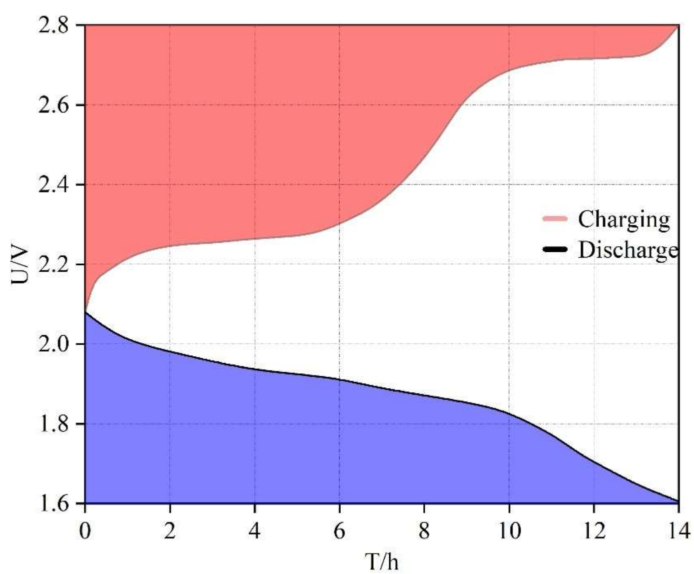

Fig. 1. Lead acid battery constant flow charging and discharge voltage change curve

2.3. Pumped energy storage

Pumped storage as a physical type of energy storage device [25], mainly relying on the gravitational potential energy of water in the upper reservoir for energy storage, the main advantage is low cost, good economy, long service life, but its disadvantages are also obvious, low energy density, slow charge/discharge response speed, can not respond quickly to the power demand of the system. Pumping energy storage consists of reversible turbine, upper reservoir and lower reservoir, the lower reservoir selection is more flexible, can be selected according to the actual geographic situation, so in this paper only need to consider the configuration of the capacity of the upper reservoir, the volume of water in the upper reservoir changes as shown below:

$$UR(t)=UR(t-1)\left(1-\frac{\tau\Delta t}{24}\right)+\left[q_{rt}^{ch}(t)-q_{rt}^{dis}(t)\right]\Delta t \tag{8}$$

$$q_{rt}^{ch}(t)=\frac{3600\eta_p P_{rt}^{ch}(t)}{\rho g h} \tag{9}$$

$$q_{rt}^{dis}(t)=\frac{3600 P_{rt}^{dis}(t)}{\rho g h \eta_t} \tag{10}$$

In the formula, Δt is the time interval of the work of the energy storage power station, which is generally taken as $\Delta t=1h$, $UR(t)$ indicates the water level of the reservoir at the moment of t, τ is the self-discharge rate of the upper reservoir, which takes the value of 0.001, $P_{rt}^{ch}(t)$ and $P_{rt}^{dis}(t)$ indicate the power of the pumped energy storage in the pumping mode and the power generation mode, $q_{rt}^{ch}(t)$ and $q_{rt}^{dis}(t)$ indicate the water flow rate of the pumped energy storage in the pumping mode and the power generation mode, η_p and η_t indicate the working efficiency of the reversible turbine in the pumping mode and the power generation mode, respectively. generation modes, ρ is the seawater density, which takes the value of $1000\mathrm{kg/m^3}$, g is the gravitational acceleration, which takes the value of $9.81m/s^2$, and h represents the height difference between the upper and lower reservoirs.

The equations for the operating efficiencies of the reversible turbine in pumping and turbine modes are as follows:

Water pump mode:

$$\eta_p=7.6392\left(\frac{q_{rt}^{ch}}{q_{rt}^{dis,0}}\right)^3-12.903\left(\frac{q_{rt}^{ch}}{q_{trt^{tis},0}}\right)^2+6.0712\left(\frac{q_{rt}^{ch}}{q_{tr}^{dis,0}}\right) \tag{11}$$

Turbo mode:

$$\eta_t=3.4523\left(\frac{q_{rt}^{dis}}{q_{rt}dis}\right)^3-9.8092\left(\frac{q_{rt}^{dis}}{q_{rt}^{dis,0}}\right)^2+8.9782\left(\frac{q_{rt}^{dis}}{q_{rt}^{dis,0}}\right)-1.7994 \tag{12}$$

where $q_{rt}^{dis,0}$ is the nominal water flow rate of the reversible turbine in turbine power generation mode.

The reversible turbine has different operating efficiencies in the pumping and power generation modes, Figure 2 shows the operating efficiency curves of the reversible turbine in the pumping and turbine modes, and the nominal water flow rate in the pumping and turbine modes is not the same, and the nominal water flow rate in the pumping mode is 53% of the nominal water flow rate in the turbine mode.

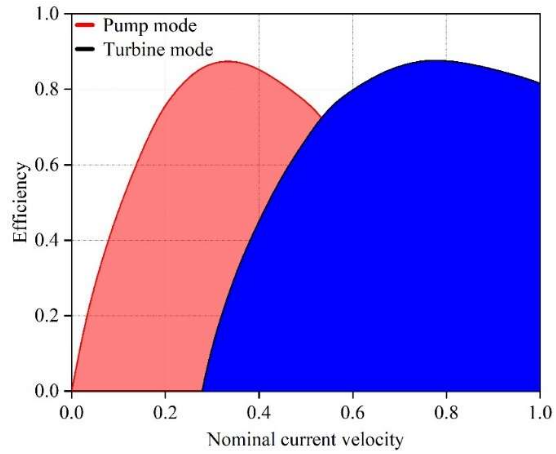

Fig. 2. Work efficiency curve of the reversible turbine pump/turbine model

2.4. Compressed air energy storage

Compressed air energy storage technology is developed based on gas turbine technology [26], Figure 3 shows the working principle diagram of gas turbine. The air is compressed by the compressor to raise the pressure into the combustion chamber, heated by fuel combustion to raise the temperature, and then the high-temperature and high-pressure flue gas enters the turbine to do work. About 2/3 of the output work of the turbine is consumed by the compressor in this process, so the overall net output work of the gas turbine is much smaller than the output work of the turbine.

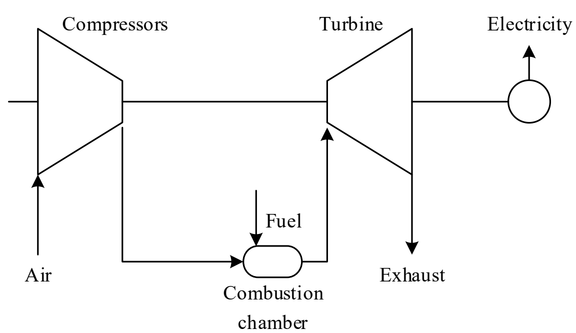

Fig. 3. Principle of gas turbine working

The conventional compressed air energy storage system consists of a compressor, storage chamber, combustion chamber, turbine, motor/generator, etc., and its system schematic is shown in Figure 4. The working principle of compressed air energy storage system is as follows: the motor is driven by the electric energy in the low time of electricity consumption, and the motor and compressor are connected together through the clutch, so that the surplus electric energy can be converted and stored in the compressed air in the air storage chamber. At the peak of electricity consumption, the generator is connected to the air turbine, and the high pressure air is heated and warmed up by the combustion chamber and then expands and does work in the turbine to drive the generator to generate electricity.

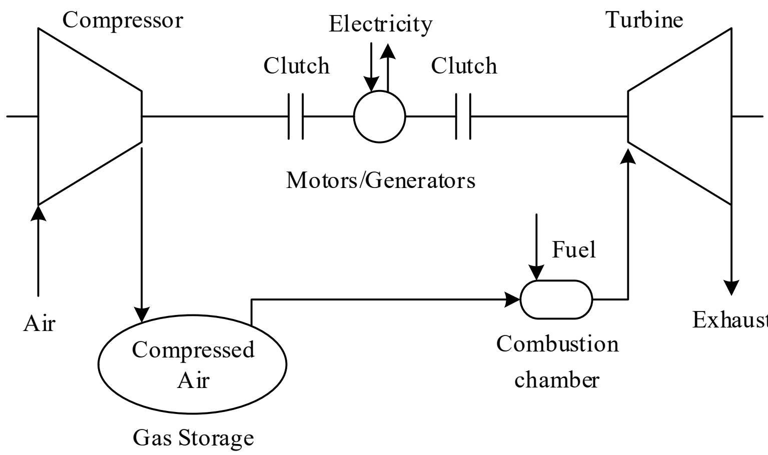

Fig. 4. Principle of compressed air storage system

The energy relationship in the compressed air energy storage process can be simply expressed as:

$$E_{store} = \frac{pV}{\gamma - 1} \tag{13}$$

Where, E_{store} is the stored energy, p is the air pressure, V is the air volume, and γ is the adiabatic index of the air.

The main components of a compressed air energy storage system generally include:

1) Compressor. Compressor in the system is generally multi-stage, add a cooling device between stages, that is, multi-stage compression stage cooling.

2) Air storage room. Large compressed air energy storage system storage room is generally an underground cavern, small systems can use a pressure vessel as a storage room.

3) Combustion chamber. The combustion chamber is used for heating compressed air by fuel combustion to improve the inlet parameters of the turbine.

4) Turbine. Used for external power output, generally for multi-stage expansion and inter-stage reheating.

5) Motor/generator; connected to the compressor and the turbine through the clutch, utilizing the input power to compress the air or outputting power to the outside through the connection of the turbine.

3. Three-dimensional modeling of energy storage power stations and the construction of virtual scenes

The construction of the virtual scene is a very important step in the comparison of different technical routes of energy storage power plants. It is difficult to compare the performance advantages and disadvantages of different technical routes of energy storage power plants in the real scene and requires a lot of manpower and material resources. However, by constructing an energy storage power plant and building a virtual scene, according to the layout and design of the actual power plant, the location of various equipment and facilities are accurately arranged in the three-dimensional scene, which can efficiently and conveniently realize the direct comparison of different technology routes. In this section, we will introduce the creation of three-dimensional models of energy storage power plant equipment and the construction of virtual scenes. Since the virtual scenes corresponding to different functions of the system are generally different, we will mainly study the construction of virtual scenes corresponding to the scene roaming function and the construction of collision detection for them.

3.1. Creation of 3D models

3.1.1. 3D Model Creation Process and Modeling Methods Through the collection of information on real-life energy storage power stations, mainly focusing on the collection of equipment size, structure, and pictures and other information, the use of 3dsMax software in accordance with the general process of three-dimensional modeling for the creation of energy storage power station models. The three-dimensional model creation process is shown in Figure 5. Due to the many types of equipment in the energy storage power station, the structure of different equipment varies greatly, using only one modeling technology can not meet the needs of three-dimensional modeling. Therefore, this paper uses a comprehensive modeling method, i.e., base modeling, faceted modeling, polygonal modeling and modifier editing model and other methods in conjunction to create a 3D model of the power plant. According to the complexity of the model structure, the power plant model is divided into simple model creation and complex model creation.

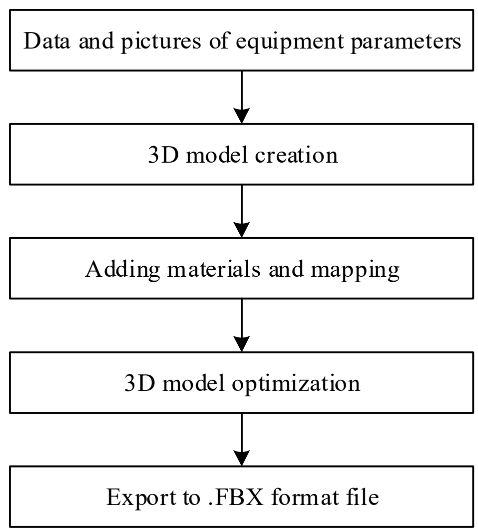

Fig. 5. 3D model creation process

1) Simple model creation For the energy storage power plant underground plant, dam and other buildings or control cabinets and other simple power plant equipment model with a certain regular shape, in the 3dsMax software mainly use the basic modeling method and the surface modeling method for three-dimensional model creation. For example, the surface of the dam is smooth, and face sheet modeling is usually used to create larger smooth objects, so use face sheet modeling to create the power station dam.
2) Complex modeling For the power station by many irregular parts of the complex equipment model, only the use of basic modeling methods can not complete the creation of the model, then also need to use polygonal modeling methods and modifiers to create complex equipment models. For example, using the polygonal modeling method, the model of the tail pipe in the water pump turbine can be created by continuously adjusting the object elements such as vertices, edges and faces on the model object. Or use the basic modeling method to create a regular geometry model, and then use the taper and stretch modifiers to create a model of the stator component in a power generating motor.

3.1.2. 3D Model Post-Processing:
1) Material and texture processing of the 3D model In order to make the 3D model easy to distinguish or make it closer to the real energy storage power plant equipment model, you can add material or texture processing to the model in 3dsMax software. Different models in the power station have different material characteristics, for example, the walls of the plant are made of cement and the ball

valves are made of metal, etc. The material editor is used to realize the addition of the model material and set the material parameters to obtain better material effects, which is closer to the actual model state in real life.

2) Three-dimensional model optimization In this paper, many equipments and buildings in the energy storage power station are modeled in 3D, and a large number of power station models are used to build the system scene, which will make the system file larger, and when the user enters the system, there may be problems such as unsmooth operation and slow loading of the scene, which will lead to a poor user experience. Therefore, in order to improve the system operation effect, it is necessary to optimize the 3D model created, mainly using the following methods: (1) Try to use the basic modeling method to create the model, with the same material or do not need to interact with the parts of the model using the functions of collapsing and attaching to integrate into a whole, without affecting the viewing effect of the premise of the model of intersecting surfaces, overlapping surfaces, and invisible surface Delete all of them. (2) Use more texture maps to show the appearance of the model, and reduce the pixels of the texture images on the premise of not affecting the viewing effect of the model.

3.1.3. Example of a three-dimensional model. The energy storage power station has a complex structure with many components, which basically uses most of the modeling methods in the comprehensive modeling method mentioned above. Figure 6 shows an example of three-dimensional modeling of some components, from which it can be seen that the three-dimensional model construction method proposed in this paper can effectively generate component models with a high degree of proximity to the real thing, which is significantly conducive to the construction of the virtual scene of the entire energy storage power station, and effectively improves the accuracy and authenticity of the results of the comparison of the performance of the different technology routes.

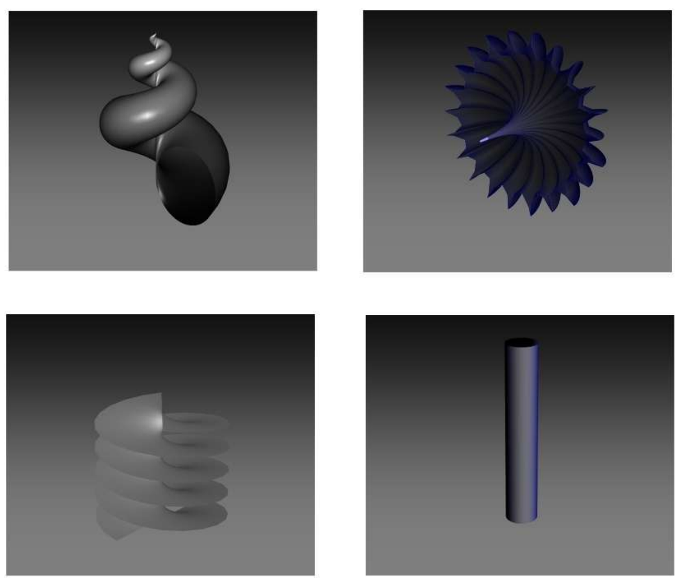

Fig. 6. Partial modeling component display

3.2. Construction of the virtual scene

3.2.1. Creation of virtual scenes:

1) Virtual Terrain Construction Find the Assets folder under the Project panel, select it and right-click on it, and choose Environment in Import Package option to import the environment resource package that comes with Unity3D into the Assets resource folder for scene construction. Click the GameObject option in the menu bar and select Terrain to complete the initial terrain creation. In the rightmost Inspector view, you can see the basic attributes of the terrain object and all the components mounted

on it, including the Transform component, Terrain component and Terrain Collision component.

There are 5 option tools in the Terrain component, which can be used to quickly create terrain, draw terrain undulations and landform textures. In the drawing of landform texture can be used to collect the power station exterior pictures, the use of Photoshop software to modify it to produce terrain mapping, so that the landform is more realistic and natural, the virtual terrain construction of the energy storage plant is shown in Figure 7. In addition, the virtual terrain also contains pumped storage power station reservoir model, the reservoir model is the most important is the design of the water surface effect. The most important thing in the reservoir model is the design of the water surface effect. Take the upper reservoir model as an example, create a plane, add a mesh renderer component to the plane, select the Shader Graphs_welat material under the material of the Mesh Renderer component, and set the parameters to complete the design of the water surface effect of the upper reservoir, and then move the plane of the water surface effect to the upper reservoir area, so that the construction of the upper reservoir model can be completed.

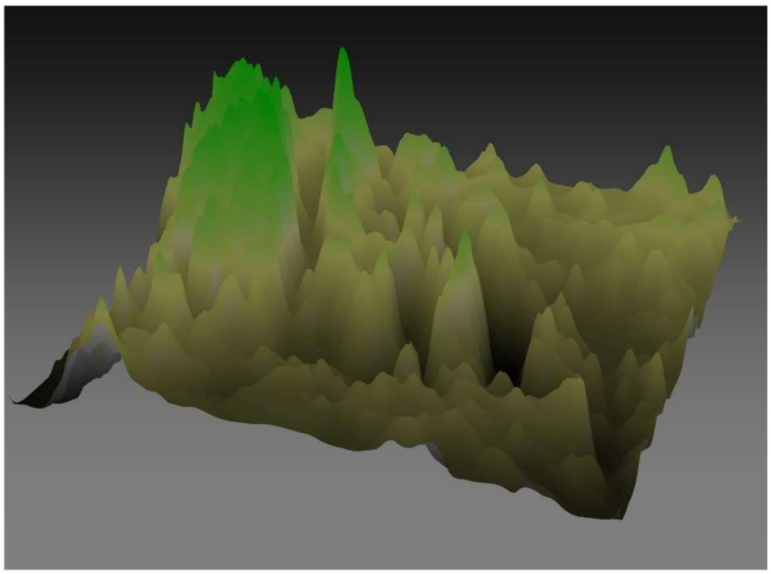

Fig. 7. Terrain model

2) Virtual Lighting Construction Lighting is a very important part of the virtual scene construction process, which determines the color and overall atmosphere of the virtual scene. Reasonable use of lighting can make the virtual scene have a very natural visual effect and improve the immersion of the system.

Unity3D engine provides four types of light sources for developers to use: parallel light, point light, spot light, and area light. Each type of light source consists of three basic attributes, namely intensity, color, and direction. The intensity and color can be set in the Inspector window, while the direction is determined by the type of light source.

The use of light sources in Unity3D needs to be configured in accordance with the actual needs of the system development. Considering the actual situation of the real-life energy storage power station, parallel light and point light sources are mainly used in the construction of its scene. Among them, the external environment of the storage power plant scene only uses parallel light to build, while the construction of the scene inside the plant uses both parallel light and point light source.

3) Sky box construction When building the external environment scene of the storage plant, in order to make the sky of the virtual scene have the same effect as the sky of the real environment, the sky box is usually used in Unity3D to set the atmosphere of the overall scene environment. If the skybox is used properly, the texture mapping edges of the terrain model may be completely integrated with the skybox, so that no matter from which angle the user observes the system scene, he or she will see a

perfect picture.

The skybox is essentially a material, so you can create your own skybox if you have specific needs for it. To create a new skybox material, click on Assets in the menu bar, find Materia in the options that pop up and click on it to get a material sphere, set the properties of the sphere to Skybox, change the properties in the Shader to Skybox/6 Sided, and select the images for all six sides.

After completing the creation of the Skybox, apply the Skybox to the scene. In the menu bar, click Window→ Rendering→ Lighting Settings, and then click Scene option in the pop-up window to assign the created Skybox material to Skybox Material property.

3.2.2. Collision testing of virtual scenes. Unity3D provides three kinds of collision test algorithms, namely, Rapid algorithm, Improved Rapid algorithm, and Improved Rapid algorithm with omitted preprocessing, in order to meet the needs of different virtual scenes. In order to select the collision test algorithms suitable for the construction of the virtual scene of the energy storage plant in this paper, this section applies the three algorithms to the preliminary construction of the virtual environment of the energy storage plant, and selects the optimal collision test algorithm through the comparison of the results.

The three algorithms are applied to the virtual scene of the energy storage power station, and the collision process of the spatial object model of the energy storage power station is shown in Figure 8. In the figure, the object models in the energy storage plant space are represented by circles and squares, respectively, and the total number of detected triangular moldings representing collisions ranges from 1376 to 9748.

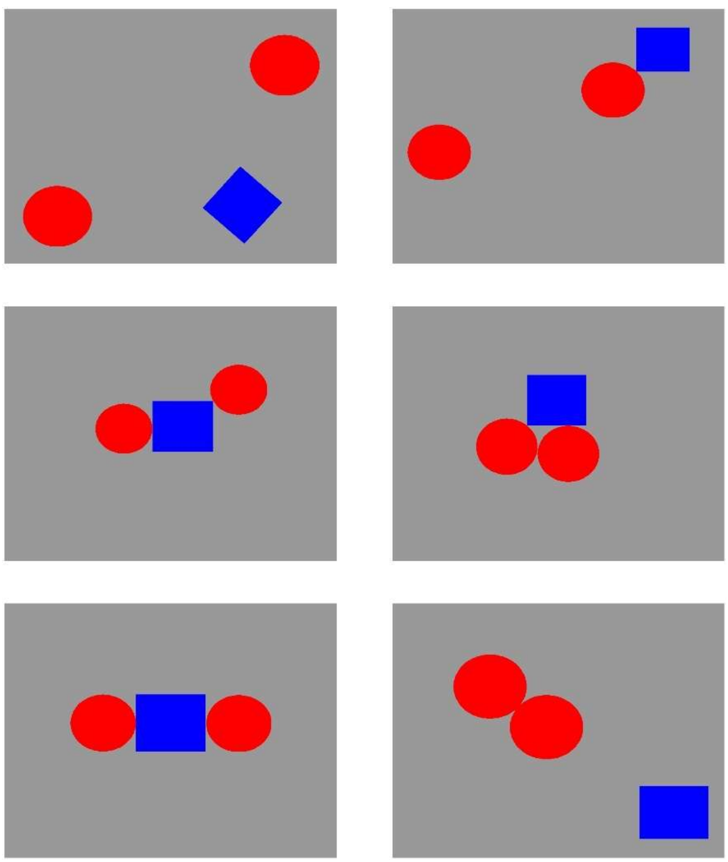

Fig. 8. Circular and square simulation the process of collision

1) When testing the algorithms in the virtual environment, the Skybox Rapid collision test was used to do the preprocessing, and the test was performed using the Separation Axis Theorem as the base premise. The collision detection time results of the three algorithms are shown in Table 1, where A, B,

and C denote the Rapid algorithm, the Improved Rapid algorithm, and the Improved Rapid algorithm that omits the preprocessing, respectively, and the three algorithms in the following sections are denoted in the same way. From the table, it can be seen that when the number of triangular mold pieces reaches 9500, the improved Rapid algorithm with omitted preprocessing reduces the collision detection time by 55.09% and 41.54%, respectively, compared with the other two algorithms, which indicates that the improved Rapid algorithm with omitted preprocessing has a significant increase in the collision detection efficiency.

Table 1. Comparison of detection time between three algorithms

Triangle modulus number	A/ms	B/ms	C/ms
1500	8.49	7.32	4.18
3500	12.87	10.98	6.42
5000	17.96	15.63	8.48
7500	22.74	21.81	11.47
9500	28.39	27.54	12.75

2) If the improved Rapid algorithm is tested by adding preprocessing first between the skybox rapid test phase, by testing with the same set of triangular molded piece data, the final results of the detection time comparison are obtained as shown in Table 2, where B* denotes the improved Rapid algorithm after adding preprocessing module. The experimental results show that the improved Rapid algorithm with preprocessing significantly increases the collision detection time compared to the original Rapid algorithm and the improved Rapid algorithm with the omission of preprocessing in the case of an increasing number of triangular mold pieces. This is mainly due to the fact that after adding the preprocessing module, the algorithm needs to preprocess the triangular mold piece data before collision detection, thus leading to a significant increase in the time consumed by the entire collision detection process.

Table 2. Comparison of detection time between three algorithms

Triangle modulus number	A/ms	B*/ms	C/ms
1500	8.49	14.83	4.18
3500	12.87	16.94	6.42
5000	17.96	22.36	8.48
7500	22.74	27.58	11.47
9500	28.39	34.92	12.75

3) Because the collision detection in this section is aimed at the virtual environment of the energy storage power station, which has a large number of components and a complex structure, when the number of triangular moldings increases significantly, the collision test detection time of the three algorithms is compared, and the results are shown in Table 3. The experimental results show that, with the significant increase in the number of triangular mold pieces, the Rapid algorithm and the improved Rapid algorithm required for the detection time are more obvious rise, omit the preprocessing of the improved Rapid algorithm collision detection time with a rise, but the rise compared to the other two algorithms is lower.

Table 3. Comparison of detection time between three algorithms

Triangle modulus number	A/ms	B/ms	C/ms
20000	71.29	69.84	35.66
30000	83.96	81.93	39.74

40000	101.48	100.75	42.13
50000	123.54	119.66	45.92
60000	158.79	153.24	48.21
70000	198.77	196.53	52.64
80000	236.41	234.32	55.87
90000	285.36	281.64	61.25
100000	320.68	319.74	66.93

In summary, based on the collision test results of the three algorithms in the virtual environment of the energy storage power plant, this paper finally chooses the improved hierarchical enclosing box (Rapid) collision test algorithm that omits preprocessing to conduct the collision test of the virtual scene of the energy storage power plant. After the complete collision test, this paper finally realizes the construction of three-dimensional model and virtual scene of the energy storage power station, which lays a solid foundation for comparing different energy storage technology routes of the energy storage power station.

4. Comparison of multiple technology routes based on virtual simulation environments

In the second part of this paper, the technology path of energy storage in energy storage power station is briefly introduced, and in the third part of the paper, the construction of three-dimensional model and virtual scene of energy storage power station is completed by using three-dimensional visualization technology. The fourth part of this section will focus on comparing the performance of the four technology paths of lithium-electron battery storage, lead-acid battery storage, pumped storage and compression storage in the virtual environment of an energy storage power plant. The first part of this section will test and analyze the energy storage performance of the four technologies in a virtual energy storage power plant. The second part focuses on comparing the energy storage capacity and efficiency of the four energy storage technologies, so as to analyze and compare the comprehensive performance of different technology routes.

4.1. Comparison of energy storage performance

4.1.1. Energy storage performance of lithium-electronic batteries. In order to better study the energy storage performance of Li-electronic batteries, CV tests were performed and the results are shown in Fig. 9. The potential window ranges from 0.0 to 2.0 V, and the scanning rate is 0.2 mV/s. The wider reduction peak located near 0.99 V during the first scan corresponds to the formation of SEI film, and will disappear in subsequent cycles indicating the formation of a stable SEI film. The reduction peak near 0.5 V in the Li-e cell is mainly attributed to the formation of LixiSi alloy. The oxidation peak near 0.3 V during anodic scanning represents the de-embedding process of lithium in graphite. The oxidation peak located near 0.55 V is attributed to the dealloying process of LixSi. Meanwhile, the CV curves of the Li-electrocells show an increase in peak intensity with the increase in scanning period, indicating the gradual activation process of the electrode materials.

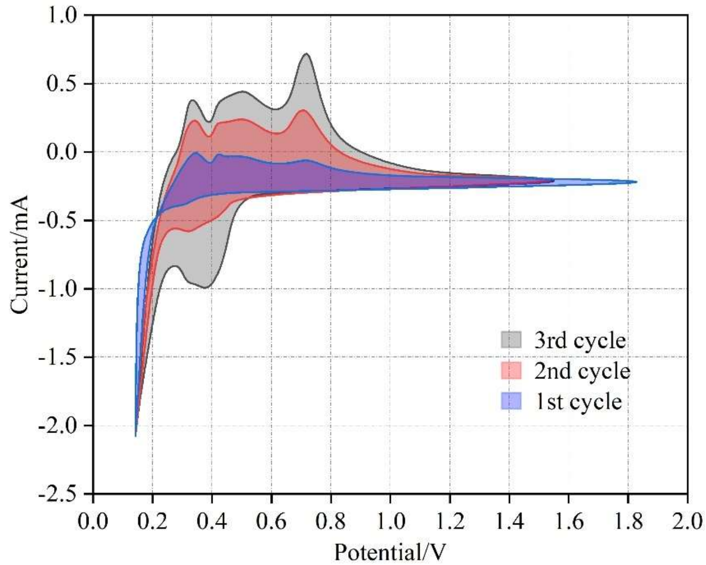

Fig. 9. The cyclic voltammetry of lithium electronic batteries

Fig. 10 shows the charging and discharging curves of the lithium e-cells cycled for 1, 3, and 8 times at a current density of 0.4 A/g. The entire right-branch portion of the curve indicates charging and the left-branch portion indicates discharging. During the first discharge, a long discharge plateau occurs when the voltage of the Li-electronic cell drops near 0 V, corresponding to the formation of a LixSi alloy with Li and Si. During charging, the long plateau located around 0.4 V corresponds to the process of Li+ de-embedding from within the LixSi alloy. From the figure, it can be seen that the first charging and discharging specific capacities of the Li-electronic battery are 1030mAg·g-1 and 1157mAg·g-1, respectively, and the first Coulombic efficiency is 89.02%, with obvious overlapping of the charging and discharging curves, which significantly highlights the excellent energy storage performance of the Li-electronic battery.

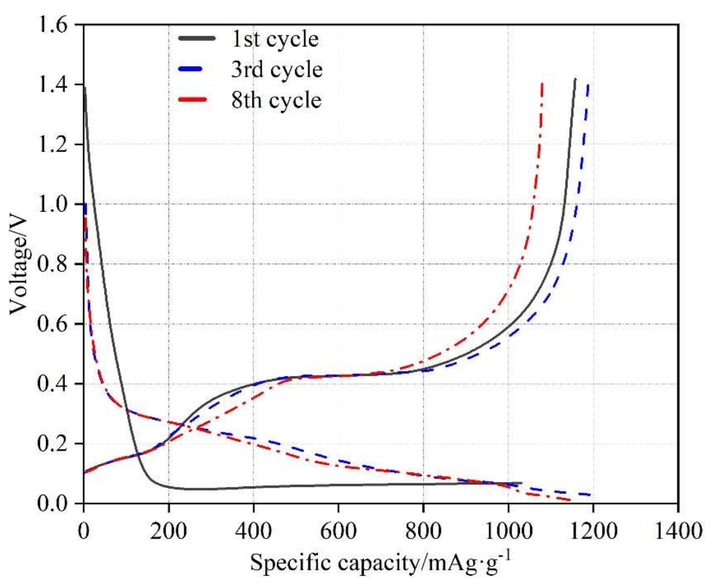

Fig. 10. Charging and discharge curve of lithium electronic battery

Figure 11 shows the AC impedance profile of the electrode material of the lithium-electronic battery before cycling, after cycling 50 and 100 laps, with the frequency range of 0~500kHZ and the amplitude of ±10mV.The AC impedance profile consists of a semicircle in the high-frequency region and a slash in the low-frequency region.The diameter of the semicircle in the high-frequency region represents the charge-transfer resistance, and a larger semicircle diameter indicates a larger charge-transfer resistance. The slope of the slash line in the low-frequency region represents the ion-port triple resistance, and the larger the slope is, the larger the Warburg resistance is. From the figure, it can be found that: with the increase in the number of cycles, the diameter of the semicircle in the high-frequency region gradually decreases, indicating that the charge transfer resistance Rct of the lithium-electronic battery continues to decrease, indicating that the charge transfer speed is increasing, at the same time, the slope of the sloping line in the low-frequency region is also increasing, indicating that the ionic diffusion resistance of the lithium-electronic battery W continues to decrease, and the speed of ionic diffusion continues to increase, which reflects that the lithium-electronic battery has good energy storage performance.

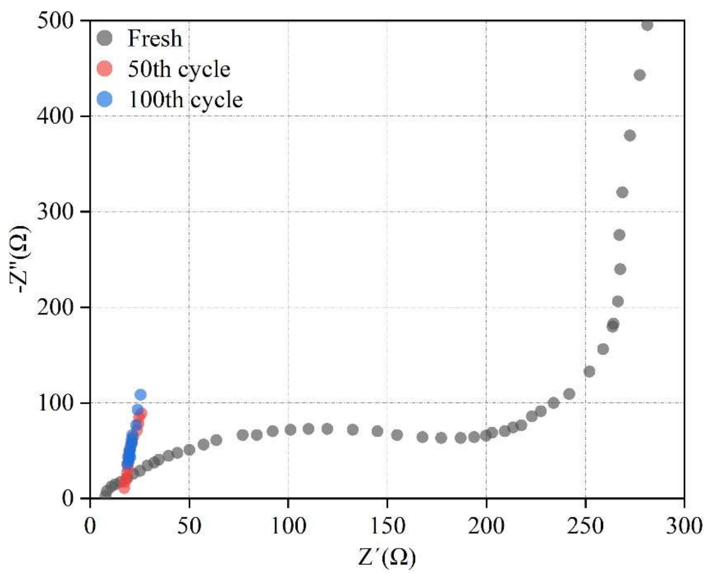

Fig. 11. The AC impedance of the lithium electronic battery

4.1.2. Lead-acid battery energy storage performance. In order to analyze the energy storage performance of the lead-acid battery, the lead-acid battery was subjected to cyclic voltammetry test. Figure 12 shows the cyclic voltammetry curve of the lead-acid battery under 1, 50 and 100 cycles. From the figure, it can be seen that the lead-acid battery does not have an oxidation peak in the first cycle, but only a reduction peak, because the surface of the lead-acid battery is covered with all PbO2 and no PbSO4. The peak current of the redox peak increases gradually as the cycle progresses. At the same time, with the increase of the number of cycles, the peak current and peak area of the redox reaction gradually increase, which is due to the fact that with the progress of the reaction in the system, the grains on the surface of the lead-acid battery gradually refine and become porous, based on the proton-electron mechanism of the lead-acid battery discharge, this multi-empty fine grain structure is conducive to the contact between H+ and HSO4- in the electrolyte and the active substance, and is also conducive to the transport of electrons, which jointly promotes the surface reaction of the lead-acid battery, thus leading to an increase in energy density.

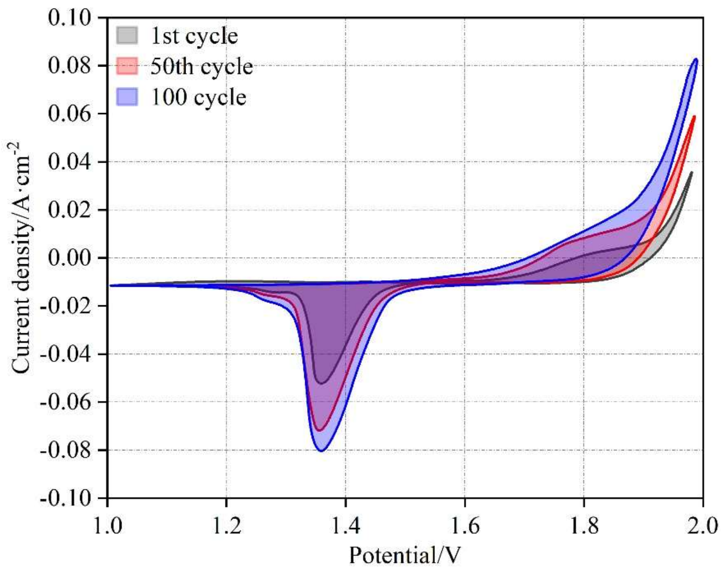

Fig. 12. Lead-acid battery cycle voltammetry curve

Figure 13 shows the charging and discharging curves of the lead-acid battery under 1, 10, 20 and 30 cycles. The upper branch of the whole curve makes the charging part, and during the charging process, the voltage gradually rises to 2.9 V. The lower branch of the charging and discharging curve is the discharging part, and as the discharging process proceeds, the discharging voltage gradually decreases, and the discharging capacity gradually increases until the discharging voltage reaches 1.5 V, and the discharging ends. The charging and discharging curves show that the discharging capacity of the lead-acid battery is 2574 mAh, 3337 mAh, 4238 mAh and 2304 mAh under four different cycle times, respectively.Meanwhile, it can also be seen from the figure that the lead-acid battery has a stronger discharging capacity and more stable energy storage performance. This is because CS can increase the active sites of the electrodes, increase the reaction activity of the electrodes, and also increase the binding force of the electrodes, which leads to the discharge performance of the lead-acid battery.

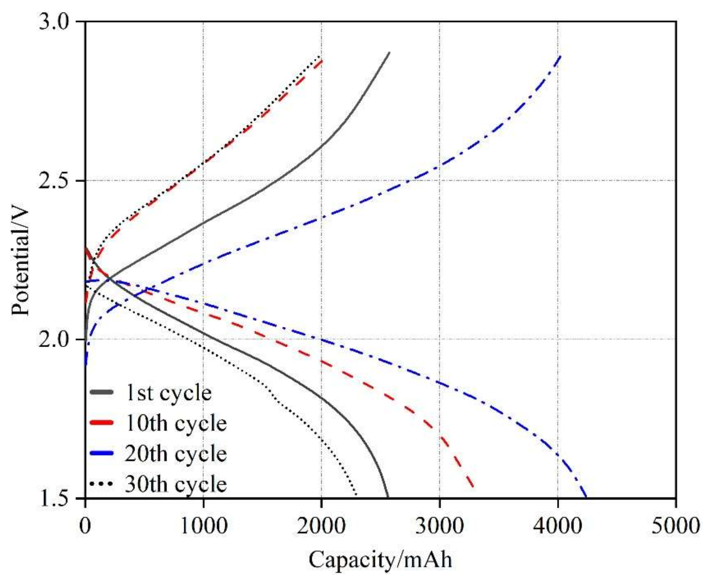

Fig. 13. The charging and discharge curve of lead-acid battery

Figure 14 shows the AC impedance spectra (Nyquist) plots of the lead-acid battery over 1, 10, 20, and 30 cycles and the equivalent circuit diagrams obtained by fitting with the system characteristics using ZSimDemo software. The equivalent circuit description code $R_s(Q(R_{ct}W))$ was used for the fitting analysis and the fitting parameters are shown in Table 4. The Nyquist plots at different cycle times consist of semicircles in the high frequency region and straight lines in the low frequency region, indicating the existence of electrochemical polarization and concentration polarization in the electrode processes of the lead-acid batteries under the four cycles. In addition, the phenomenon of impedance semicircle rotation appears in the Nyquist plot making the center of the semicircle fall below the X-axis, indicating the presence of dispersion effect. In the equivalent circuit, R_s is the solution resistance and the normal phase element Q represents the non-ideal capacitor, the occurrence of dispersion effect is due to the roughness of the surface of the lead-acid battery which causes the variation of the double capacitance layer and inhomogeneity of the power plant. R_{ct} is the charge transfer resistance for the reaction process in the lead-acid battery, corresponding to the diameter of the semicircle in the Nyquist diagram. W represents the concentration polarization resistance, which is the Warburg impedance due to the migration of H+ and HSO4- during the liquid phase mass transfer, and corresponds to the straight line portion of the Nyquist diagram. Comparison of the charge transfer resistance shows that as the number of cycles increases the R_{ct} value is decreasing and the charge transfer process is more easily carried out, thus the energy storage performance of the lead-acid battery is rising.

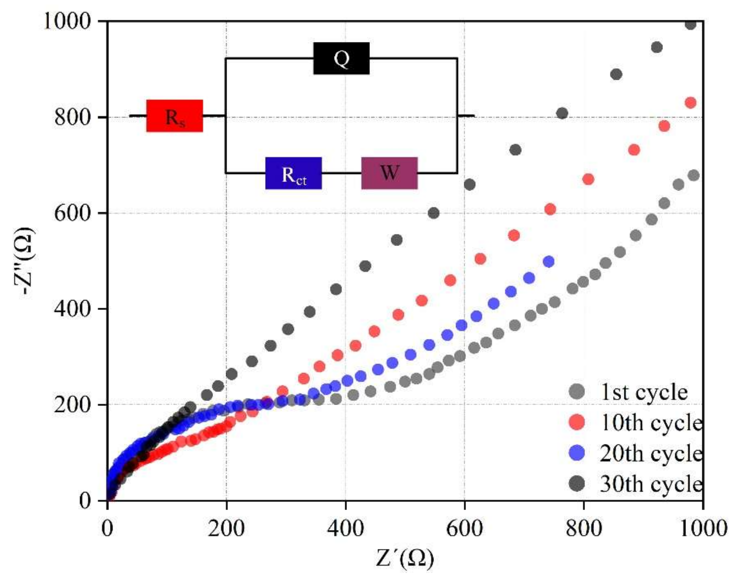

Fig. 14. AC impedance and equivalent circuit of lead-acid battery

Table 4. Equivalent circuit component parameters of lead-acid batteries

Cycle number	Rs/Ω·cm2	Q/Ω-1·cm2	N	Rct/Ω·cm2	W/Ω·cm2
1st	0.6432	1.528×10-4	0.9135	336.42	2.386×10-3
10th	0.5976	6.207×10-4	0.9648	298.35	1.257×10-3
20th	0.6135	3.894×10-4	0.8917	178.64	3.306×10-3
30th	0.6178	1.583×10-4	0.9024	57.19	9.683×10-3

4.1.3. Pumped energy storage performance. When the rotational speed of the turbine rises from 5000r/min to 8000r/min, the charging energy is measured on the grid side, DC side and motor side, respectively; when the rotational speed of the turbine falls from 8000r/min to 5000r/min, the discharging energy is measured on the grid side, DC side and motor side, respectively; the operating power of the pumped storage device is 480kW, and the operating power of a single pumped storage device is 160kW. After several measurements, the cycle efficiency of the pumped storage device is calculated for the grid side, DC side and motor side respectively. The calculation process is shown in

Tables 5-7, where E_c indicates the grid-side charging energy, E_d indicates the grid-side discharging energy, E'_c indicates the DC-side charging energy, E'_d indicates the DC-side discharging energy, E''_c indicates the motor-side charging energy, and E''_d indicates the motor-side discharging energy. From the table, it can be seen that the grid-side cycling efficiency of the pumped storage device is $\eta_G = 86.34\%$, the DC-side cycling efficiency is $\eta_D = 89.22\%$, and the electrode-side cycling efficiency is $\eta_M = 91.06\%$. Thus, there is a charging/discharging efficiency loss of $1-(\eta_G/\eta_D)=3.23\%$ for the grid-side converter, and a charging/discharging efficiency loss of $1-(\eta_D/\eta_M)=2.02\%$ for the motor-side converter.

Table 5. Circulation efficiency of grid side pumping energy storage device

Cycle number	Test content/(r·min-1)	Lateral energy/(W·h)	$E_c/(W\cdot h)$	$E_d/(W\cdot h)$	$\eta_G/\%$
1	Charging:5000→8000	-23768.64	-22204.99	19171.18	86.34
	Discharge:8000→5000	19092.57			
2	Charging:5000→8000	-21584.71			
	Discharge:8000→5000	19163.24			
3	Charging:5000→8000	-21382.93			
	Discharge:8000→5000	19164.49			
4	Charging:5000→8000	-22306.83			
	Discharge:8000→5000	19197.66			
5	Charging:5000→8000	-21981.84			
	Discharge:8000→5000	19237.96			

Table 6. Circulation efficiency of DC side pumping energy storage device

Cycle number	Test content/(r·min-1)	DC side energy/(W·h)	$E'_c/(W\cdot h)$	$E'_d/(W\cdot h)$	$\eta_D/\%$
1	Charging:5000→8000	-9748.23	-9673.11	8630.33	89.22
	Discharge:8000→5000	8356.94			
2	Charging:5000→8000	-9628.59			
	Discharge:8000→5000	8352.71			
3	Charging:5000→8000	-9639.53			
	Discharge:8000→5000	8496.58			
4	Charging:5000→8000	-9660.86			
	Discharge:8000→5000	8397.21			
5	Charging:5000→8000	-9688.33			
	Discharge:8000→5000	9548.19			

Table 7. Circulation efficiency of motor side pumping energy storage device

Cycle number	Test content/(r·min-1)	DC side energy/(W·h)	$E''_c/(W\cdot h)$	$E''_d/(W\cdot h)$	$\eta_M/\%$
1	Charging:5000→8000	-9326.48	-9454.21	8909.10	91.06
	Discharge:8000→5000	8573.29			
2	Charging:5000→8000	-9546.13			
	Discharge:8000→5000	8579.58			
3	Charging:5000→8000	-9438.91			

	Discharge:8000→5000	8672.11			
4	Charging:5000→8000	-9517.38			
	Discharge:8000→5000	8576.93			
5	Charging:5000→8000	-9442.17			
	Discharge:8000→5000	8643.57			

When the rotational speed of the turbine rises from 5000r/min to 8000r/min, the actual power on the grid side, DC side and motor side are measured respectively, and when the rotational speed of the turbine falls from 8000r/min to 5000r/min, the actual power on the grid side, DC side and motor side are measured respectively, and the test power of pumping and storage device is set to be 480kW, and the single pumping and storage device's The test power of single pumped energy storage device is 160kW. After several measurements, the conversion efficiencies of the grid-side converter and the machine-side converter are calculated separately, and the results are shown in Tables 8-Table 9, where η_c' indicates the grid-side converter charging efficiency and η_d' indicates the grid-side converter discharging efficiency. η_c'' is the motor-side charging efficiency, and η_d'' is the motor-side converter discharge efficiency. From the table, it can be seen that the loss of the converter on the grid side is about 3.24%, and the loss of the converter on the motor side is about 2.22%, which is basically the same as the result through energy measurement.

Table 8. Conversion efficiency of converter on grid side

Cycle number	Test content/(r·min-1)	Grid side power/W	DC side power/W	Conversion efficiency/%
1	Charging:5000→8000	-384753	-374283	97.28
	Discharge:8000→5000	362897	375426	96.66
2	Charging:5000→8000	-385946	-378594	98.10
	Discharge:8000→5000	365871	375326	97.48
3	Charging:5000→8000	-374983	-371971	99.20
	Discharge:8000→5000	369572	370897	99.64
4	Charging:5000→8000	-378326	-376321	99.47
	Discharge:8000→5000	365468	370138	98.74
5	Charging:5000→8000	-380241	-374893	98.59
	Discharge:8000→5000	367348	372386	98.65
$\eta_c' / \%$	98.53			
$\eta_d' / \%$	98.23			

Table 9. Conversion efficiency of converter on motor side

Cycle number	Test content/(r·min-1)	DC side power /W	Motor side power/W	Conversion efficiency/%
1	Charging:5000→8000	-183326	-182347	99.47
	Discharge:8000→5000	197328	198673	99.32
2	Charging:5000→8000	-182478	-178348	97.74
	Discharge:8000→5000	196571	197386	99.59
3	Charging:5000→8000	-189746	-189523	99.88
	Discharge:8000→5000	197324	198369	99.47
4	Charging:5000→8000	-185743	-183284	98.68
	Discharge:8000→5000	191378	195329	97.98
5	Charging:5000→8000	-188432	-187327	99.42
	Discharge:8000→5000	191654	196872	97.35
$\eta_c''/\%$	99.04			
$\eta_d''/\%$	98.74			

4.1.4. Compressed air energy storage performance. The parameters of the compressed air energy storage device are input into the virtual environment of the energy storage power plant, and the average of the results of the three sets of experimental tests is used as a benchmark to explore the energy storage performance of the compressed air device.

Table 10 shows the simulation results and relative errors of the compression stage. Comparing the simulation results with the actual results, it can be seen that the error in the compression stage is between 0.62% and 4.73%, and the simulation results are in good agreement with the actual results. The storage pressure of the simulation results is 9.76MPa, which is 1.25% lower than the actual value, the storage time is 3.83h, which is 4.73% lower than the actual value, and the compression power consumption is 221.76kWh, which is 0.62% lower than the actual value. This is because the pressure in the storage tank gradually rises during the compression process, and the compressor discharge pressure gradually rises with the rise of the pressure in the storage tube, and the power is smaller than the rated power due to the fact that the third and fourth stage compressor compression process pressure is lower than the rated pressure for a long period of time during the actual operation.

Table 10. Simulation and relative error of compression phase

Parameter	Unit	Analog value	Actual value	Relative error/%
Energy storage pressure	MPa	9.46	9.58	1.25
Energy storage time	h	3.83	4.02	4.73
Compressive energy consumption	kWh	221.76	223.15	0.62

Table 11 shows the simulation results and relative errors for the expansion generation stage. Comparing the simulation results with the actual results, the errors are between 1.02% and 3.85%, and the simulation results are in good agreement with the actual results. In the simulation, the inlet air temperature of the primary turbine is 132.78°C, which is 2.16% higher than the actual value, and the outlet air temperature is 61.46°C, which is 2.10% lower than the actual value. The inlet temperature of the secondary turbine is 126.49°C, which is 1.02% higher than the actual value, and the outlet air temperature is 38.71°C, which is 2.32% lower than the actual value. The simulated values of temperature difference between the inlet and outlet of the primary turbine and the temperature difference between the inlet and outlet of the secondary turbine are larger than the actual values, which are analyzed as the reason that the thermal efficiency of the turbine decreases in actual operation, the power generating power per unit mass of air decreases, and the enthalpy difference between the inlet and outlet air decreases. The simulated value of turbine power generation is 115.83kW, which is 1.53% higher than the actual value, and the power generation time is 0.27h, which is 3.85% higher than the actual value. This is due to the fact that the actual location is located in a high altitude area, the actual energy storage of the turbine air consumption increases, the turbine output of the same power needs to consume more air mass, in the case of the total storage energy remains unchanged, the actual system of the power generation power and power generation time to be reduced.

Table 11. Simulation results and relative error of the expansion generation stage

Parameter	Unit	Analog value	Actual value	Relative error/%
Primary turbine intel air temperature	℃	132.78	129.97	2.16
Primary turbine outlet air temperature	℃	61.46	62.78	2.10
Secondary turbine intel air temperature	℃	126.49	125.21	1.02
Secondary turbine outlet air temperature	℃	38.71	39.63	2.32
Turbine power generation	kW	115.83	114.09	1.53
Power generation time	h	0.27	0.26	3.85

Table 12 shows the simulation results and relative errors of the energy storage stage. Comparing the simulation simulation results of the photovoltaic heat collection/storage stage and the actual results, the relative error is between 1.44% and 1.72%, and the simulation results are in good agreement with the actual results. In the energy storage stage, the simulated value of the final temperature of the generator is 183.58°C, which is 1.72% higher than the actual value, and the reason for this is that the heat loss from the cold to the hot state of the compressed air energy storage device is unavoidable and the proportion of the heat loss is large, and at the same time, it takes a period of time from the preheating of the heat exchanger to the normal operation, which leads to the poorer performance of the heat exchanger. The simulated value of the final motor temperature is 59.36°C, which is 1.44% lower than the actual value.

Table 12. Simulation results and relative error of energy storage phase

Parameter	Unit	Analog value	Actual value	Relative error/%
Generator final temperature	℃	183.58	180.47	1.72
Motor final temperature	℃	59.36	60.23	1.44

In summary, the errors of the simulated values of the compressed air energy storage device in each operation stage are within 5%, so it can be concluded that the compressed air energy storage has a good energy storage performance.

4.2. Comparison of energy storage indicators

4.2.1. Comparison of energy storage capacity. In the previous section, the energy storage performance of different energy storage power plant technology routes, such as lithium-electron battery energy storage, was elaborated in detail. In this section, we will focus on measuring the energy storage performance of different technology routes through the two measures of energy storage capacity and energy storage efficiency, so as to find the energy storage technology routes suitable for the virtual environment of the energy storage power plant constructed in this paper.

Figure 15 shows the comparison of the energy storage capacity of four different technology routes in 2023, and (a)-(d) denote the lithium-ion battery energy storage, lead-acid battery energy storage, pumped water energy storage and compressed air energy storage, respectively. As can be seen from the figure, the net energy storage capacity of the four technology routes is 728.99 MW, 724.18 MW, 461.50 MW, and 393.45 MW, respectively. Although the net energy storage capacity of lithium-ion battery energy storage is more than that of lead-acid battery energy storage, it can be clearly seen from the figure that the fluctuation of lithium-ion battery energy storage capacity is more than that of lead-acid battery energy storage in different months, which indicates that the lithium-ion battery energy storage performance is not as stable as lead-acid battery. While pumped water energy storage and compressed air energy storage are more stable in energy storage performance, their net energy storage capacity decreases significantly compared with lead-acid batteries. Therefore, in the virtual environment of the energy storage power station constructed in this paper, the lead-acid battery has stable energy storage performance and large energy storage capacity, so it is more suitable for the virtual environment of this paper.

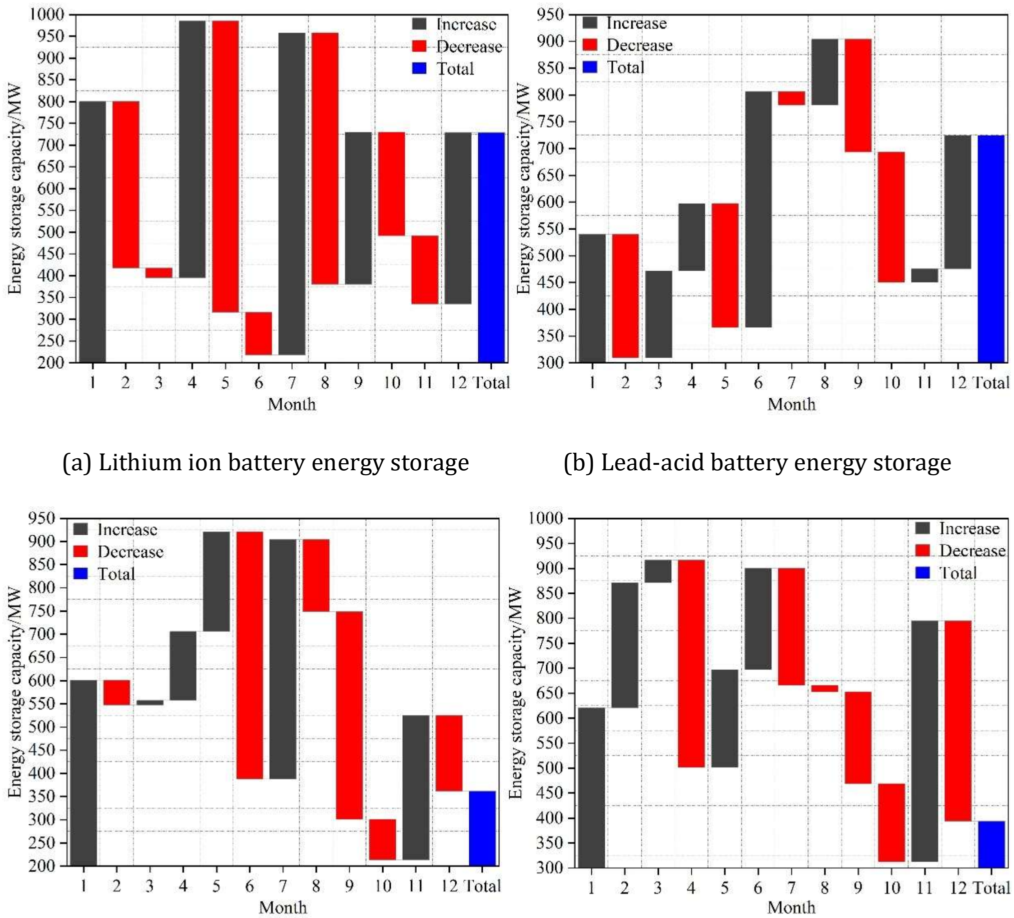

(a) Lithium ion battery energy storage (b) Lead-acid battery energy storage

(c) Pumped energy storage (d) Compressed air energy storage

Fig. 15. Comparison of storage capacity between different technical routes

4.2.2. Comparison of energy storage efficiency. The energy storage efficiency can be used to measure the energy storage losses of different technology routes in an energy storage power plant, and is valuable for measuring the performance of different technology routes. Energy storage efficiency is usually expressed as a percentage of the ratio of discharge to charge. Table 13 shows the comparison of energy storage efficiency of four different technology routes in four quarters in 2023, R1-R4 in the table represent four technology routes of lithium-ion battery storage, lead-acid battery storage, pumped storage and air compression storage, respectively, and the data in the table shows that the average values of energy storage efficiency of the four different routes in four quarters are 85.42%, 99.71%, 64.41%, and 69.87%, respectively. Compared with the two chemical energy storage methods of lithium-ion battery and lead-acid battery, the two physical energy storage methods of pumped water energy storage and compressed air energy storage have lower energy storage efficiency and higher loss in the energy storage process. In the two chemical energy storage methods, the four quarterly energy storage efficiency of lead-acid ion battery is 99.52%, 99.60%, 99.75% and 99.96% respectively, which are all above 99%, and the average value of its energy storage efficiency is increased by 14.29% compared with that of lithium-ion battery. It shows that the use of lead-acid battery energy storage process, energy loss is small, energy storage performance is high, and at the same time reconfirms that the lead-acid battery energy storage is the most suitable for the virtual environment of the energy storage power station built in this paper.

Table 13. The efficiency contrast of different technical routes

Routes	Quarter	Charging capacity/kWh	Discharge quantity/kWh	Efficiency/%	Mean/%
R1	1	-193687	164483	84.92	85.42
	2	-183724	150348	81.83	
	3	-196478	176239	89.7	
	4	-195214	166382	85.23	
R2	1	-193687	192748	99.52	99.71
	2	-183724	182998	99.6	
	3	-196478	195986	99.75	
	4	-195214	195138	99.96	
R3	1	-193687	128673	66.43	64.41
	2	-183724	114928	62.55	
	3	-196478	127154	64.72	
	4	-195214	124837	63.95	
R4	1	-193687	138452	71.48	69.87
	2	-183724	124673	67.86	
	3	-196478	137983	70.23	
	4	-195214	136471	69.91	

5. Conclusion

In this paper, the 3D model and virtual simulation environment of the energy storage power station are constructed by 3dsMax and with Unity3D software, and the performance of different energy storage technology routes, such as lithium-electronic battery storage, lead-acid battery storage, pumped water storage and compressed air storage, is compared and analyzed in the virtual environment.

The net energy storage capacity of the four energy storage routes in 2023 is 728.99 MW, 724.18 MW, 461.50 MW, and 393.45 MW, respectively. lithium-electronic battery has the highest net energy storage capacity, but the fluctuation of the energy storage capacity value in each month is drastic, while pumped water storage and compressed air storage have less fluctuation of the energy storage capacity value in different months, but their losses in the process of energy storage are larger, resulting in a lower final net energy storage capacity. In contrast, the net energy storage capacity of the lead-acid battery is 4.81 MW less than that of the lithium-ion battery, but the fluctuation of the energy storage capacity of the lead-acid battery is significantly less than that of the lithium-ion battery. It shows its stable energy storage performance and good energy storage performance in the virtual environment of this paper. Meanwhile, the energy storage efficiencies of lead-acid batteries in the four quarters are

99.52%, 99.60%, 99.75%, and 99.96%, respectively, with average energy storage efficiencies of 14.29%, 35.30%, and 29.84% higher than those of the other three energy storage technology routes. This further illustrates the superior performance of lead-acid batteries in the virtual simulation environment of the energy storage power plant in this paper.

References

[1] Chen, X., & Chen, X. (2021). Data visualization in smart grid and low-carbon energy systems: A review. International Transactions on Electrical Energy Systems, 31(7), e12889.

[2] Rodrigues, N., Netzel, R., Ullah, K. R., Burch, M., Schultz, A., Burger, B., & Weiskopf, D. (2017, August). Visualization of time series data with spatial context: Communicating the energy production of power plants. In Proceedings of the 10th International Symposium on Visual Information Communication and Interaction (pp. 37-44).

[3] Pan, J., Qi, H., & Zheng, R. (2021, April). Massive power grid operational status data analysis system for 3D visualization. In 2021 IEEE Asia-Pacific Conference on Image Processing, Electronics and Computers (IPEC) (pp. 196-203). IEEE.

[4] Li, Y., Luo, J., Dong, C., & Feng, Y. (2022, December). 2D/3D Visualization Realization of Power Grid Operation Monitoring System Based on Big Data. In International Conference on Big Data Analytics for Cyber-Physical System in Smart City (pp. 337-345). Singapore: Springer Nature Singapore.

[5] Guo, D., Pu, C., Li, M., Zhang, W., Zhao, J., & Arlia, L. A. (2017, April). Application and study of 3D visualization model on nuclear power plant construction. In IOP Conference Series: Earth and Environmental Science (Vol. 61, No. 1, p. 012023). IOP Publishing.

[6] Peng, H., Wang, Q., Yang, Y., & Bi, M. (2016, April). Research and application of digital 3D modeling technology in substation monitoring. In Proceedings of the 3rd International Conference on Engineering Technology and Application (ICETA 2016), Kyoto, Japan (pp. 28-29).

[7] Jiang, A., Su, L., & Si, W. (2024, February). Research on 3D visualization technology of substation grounding network based on BIM and digital twin. In Ninth International Conference on Energy Materials and Electrical Engineering (ICEMEE 2023) (Vol. 12979, pp. 1651-1657). SPIE.

[8] Liu, J., Lu, X., Zhou, Y., Cui, J., Wang, S., & Zhao, Z. (2021, November). Design of photovoltaic power station intelligent operation and maintenance system based on digital twin. In 2021 6th International Conference on Robotics and Automation Engineering (ICRAE) (pp. 206-211). IEEE.

[9] Sato, Y., & Terasaka, Y. (2022). Radiation imaging using an integrated Radiation Imaging System based on a compact Compton camera under unit 1/2 exhaust stack of Fukushima Daiichi Nuclear Power Station. Journal of Nuclear Science and Technology, 59(6), 677-687.

[10] Yang, J., Wu, F., Lai, E., Liu, M., Liu, B., & Zhao, Y. (2021). Analysis of visualization technology of 3d spatial geographic information system. Mobile Information Systems, 2021(1), 9173281.

[11] Lee, H., & Cha, W. C. (2019). Virtual reality-based ergonomic modeling and evaluation framework for nuclear power plant operation and control. Sustainability, 11(9), 2630.

[12] Wang, H., Huang, Z., Zhang, X., Huang, X., wei Zhang, X., & Liu, B. (2022). Intelligent power grid monitoring and management strategy using 3D model visual computation with deep learning. Energy Reports, 8, 3636-3648.

[13] Yan, J., Zhou, J., Li, Y., Cao, X., Sun, Y., & Liu, B. (2022, March). Research on intelligent pumped storage power station based on digital twins technology. In Journal of Physics: Conference Series (Vol. 2237, No. 1, p. 012022). IOP Publishing.

[14] Jin, F., Wang, H., Luo, Y., Presas, A., Bi, H., Wang, Z., ... & Yang, X. (2023). Visualization research of energy dissipation in a pump turbine unit during turbine mode's starting up. Renewable Energy, 217, 119172.

[15] Xia, P. (2021, April). The Function and Application of 3D Visualization in Power Operation and Maintenance System. In Journal of Physics: Conference Series (Vol. 1881, No. 3, p. 032018). IOP Publishing.

[16] Dongyun, D., Zheng, W., Yimin, Y., Zhongqing, S., Huisheng, Y., & Weiyun, J. (2022, December). Research on Intelligent Online Operation and Maintenance System of 3D Visualization Hydrogen Production and Energy Storage Power Station. In 2022 4th International Conference on Smart Power & Internet Energy Systems (SPIES) (pp. 2128-2133). IEEE.

[17] Li, Y., Zhang, H., & Zhang, Q. (2021). A framework for interactive online 3d visualization of electric information. In Journal of Physics: Conference Series (Vol. 1757, No. 1, p. 012170). IOP Publishing.

[18] Gan, X., Wu, X., Xu, Z., & Xiao, H. (2023, May). Power transmission and transformation project 3D visualization system design research. In Second International Conference on Electronic Information Engineering, Big Data, and Computer Technology (EIBDCT 2023) (Vol. 12642, pp. 768-775). SPIE.

[19] Tang, X., Fang, C., Zhao, K., & Huang, K. (2023, December). Visualization Technology and Application of 3D Grid Wiring Diagram Based on Unity. In 2023 3rd International Conference on Electrical Engineering and Control Science (IC2ECS) (pp. 879-884). IEEE.

[20] Wang, H., Li, D., Yang, Z., Zhang, Y. N., Zhang, Y., & Xu, J. (2018, November). Research on recognition and 3-D visualization of key equipment in NPP based on AR technology. In 2018 International Conference on Power System Technology (POWERCON) (pp. 4661-4667). IEEE.

[21] Dai, E., & Wang, Q. (2022, January). Simulation Design of Dynamic Visualization System Based on Wind Power Station. In ICETIS 2022; 7th International Conference on Electronic Technology and Information Science (pp. 1-6). VDE.

[22] Qian, P., Yu, M., Zhang, S., Jiang, S., Tang, J., & Dong, S. (2024, February). Design and Application Analysis of Multi-Station Fusion Visualization System Based on Digital Twin. In 2024 IEEE International Conference on Big Data & Machine Learning (ICBDML) (pp. 91-96). IEEE.

[23] Yuan Fan,Zepei Zhang,Guozhi Yang,Tianhong Pan,Jiaqiang Tian,Mince Li... & Peng Wang. (2025). A comparative study of modeling and parameter identification for lithium-ion batteries in energy storage systems. Measurement116263-116263.

[24] Aravind Baby,Abdelilah Asserghine,Elizabeth Gao,Huimin Zhao & Joaquín Rodríguez López. (2025). A simple room-temperature refurbishment method for sulfated lead-acid batteries using ammonium acetate treatment. Journal of Power Sources235812-235812.

[25] Weidong Guan,Jinshuai Zhang,Peng Wang,Ning Zhou,Bowen Shang,Changhao Xu... & Ran Tao. (2025). Head variation adaptive control of small-scale doubly-fed pumped storage units. Electric Power Systems Research111277-111277.

[26] Firdovsi Gasanzade & Sebastian Bauer. (2025). Approximating coupled power plant and geostorage simulations for compressed air energy storage in porous media. Applied Energy125070-125070.